

## REPORT DOCUMENTATION PAGE

Public reporting burden for this collection of information is estimated to average 1 hour per response, including the time for reviewing instructions, searching existing data sources, gathering and maintaining the data needed, and completing and reviewing this collection of information. Send comments regarding this burden estimate or any other aspect of this collection of information, including suggestions for reducing this burden, to Washington Headquarters Services, Directorate for Information Operations and Reports (0704-0188), 1215 Jefferson Davis Highway, Suite 1204, Arlington, VA 22202-4302, and to the Office of Management and Budget, Paperwork Project Director (0704-0188), 1215 Jefferson Davis Highway, Suite 1204, Arlington, VA 22202-4302. Other provisions of law, no person shall be subject to any penalty for failing to comply with a collection of information if it does not display a currently valid OMB control number.

1. REPORT DATE (DD-MM-YYYY) 04/30/01		2. REPORT TYPE Final Report		3. DATES COVERED (From - To) 07/15/96 - 03/14/00	
4. TITLE AND SUBTITLE Ultrashort Pulse, Monolithic Modelocked Lasers for WDM Systems				5a. CONTRACT NUMBER F49620-96-1-0371	
				5b. GRANT NUMBER	
				5c. PROGRAM ELEMENT NUMBER	
6. AUTHOR(S) P. Daniel Dapkus				5d. PROJECT NUMBER	
				5e. TASK NUMBER	
				5f. WORK UNIT NUMBER	
7. PERFORMING ORGANIZATION NAME(S) AND ADDRESS(ES) Department of Electrical Engineering - Electrophysics University of Southern California Los Angeles, CA 90089-0243				8. PERFORMING ORGANIZATION REPORT NUMBER	
9. SPONSORING / MONITORING AGENCY NAME(S) AND ADDRESS(ES) Air Force Office of Scientific Research 801 North Randolph Street, Room 732 Arlington, VA 22203-1977				10. SPONSOR/MONITOR'S ACRONYM(S)	
				11. SPONSOR/MONITOR'S REPORT NUMBER(S)	
12. DISTRIBUTION / AVAILABILITY STATEMENT  Approved for public release: Distribution unlimited					
13. SUPPLEMENTARY NOTES					
14. ABSTRACT A program of research to investigate the use of modelocked lasers as sources for WDM systems is reported. The objective of the program was to demonstrate modelocked lasers with ultrashort pulse widths that contain as many as 16 phase locked longitudinal modes. Analysis was carried to understand the role of self phase modulation on the spectral range of modes that could be phase locked in such a device. The results of the analysis suggest that this fundamental limitation must be addressed by engineering the round trip phase dispersion over a broad spectral range to achieve a broad enough spectral width to successfully fabricate monolithic WDM sources that will compete with current technology. Experimental monolithic passively modelocked colliding pulse modelocked lasers were constructed during the course of the program. Devices with 1.2 psec pulse width operating with a pulse repetition rate of ~ 40 GHz were demonstrated. These devices had longitudinal mode spectra containing up to 16 phase locked modes but the amplitude variation over the mode spectrum precluded their use as independent WDM spectral sources.					
15. SUBJECT TERMS Optical Communications, Photonics, Wavelength Division Multiplexing, Modelocked Lasers, Semiconductor Lasers					
16. SECURITY CLASSIFICATION OF:			17. LIMITATION OF ABSTRACT  UL	18. NUMBER OF PAGES  28	19a. NAME OF RESPONSIBLE PERSON P. Daniel Dapkus
a. REPORT Unclassified	b. ABSTRACT Unclassified	c. THIS PAGE Unclassified			19b. TELEPHONE NUMBER (include area code) (213) 740-4414

Standard Form 298 (Rev. 8-98)  
Prescribed by ANSI Std. Z39.18

20010625 122

## Introduction

This report describes the result of an experimental and theoretical study of the use of mode locked lasers as multiple wavelength sources for WDM systems. The effort involved modeling of mode locked semiconductor lasers with special emphasis on understanding the role of self phase modulation on the locking stability and range of passively mode locked lasers. Our objective in undertaking this work was to extend the spectral range of mode locked lasers so that several modes ( $\sim 16$ ) could be locked to produce a manifold of equally spaced laser wavelengths to be used in a WDM system.

Progress in this program was severely hampered by the untimely illness of the graduate student involved in the program. Approximately 1.5 - 2 years into the program, the student who was carrying out the experimental device work suffered a debilitating illness that ended his graduate work and severely truncated the experimental effort. This prevented us from achieving some of the program objectives listed below. However, we were able to accomplish some of the program objectives and to define the likelihood of success for the approach originally proposed.

Mode locking is effected in a laser by modulating the net gain in a laser at a frequency equal to the frequency separation of the longitudinal modes of the laser. This has the effect coupling nearest neighbor or next nearest neighbor modes together and locking the phase of these modes to one another. The net effect of this phase locked system of modes is that they behave as a collective ensemble of photons that reaches threshold at a value lower than would occur for a conventional single mode operation. The coherent phase locked ensemble of modes in the frequency domain leads to a repetitive short pulse operation in the time domain. The repetition frequency of the pulses is equal to the round trip frequency of the photons in the cavity,  $c/(2nL)$ . In principle such a laser can be used as a high repetition rate short pulse generator if all of the coherent modes are used in the output pulse or if the individual modes are filtered separately from the output as a CW multi-wavelength source. In either form, this laser is useful as a signal generation source for photonic systems. In principle, because the gain spectrum of a semiconductor laser is so wide, the device should be able to exhibit many modes ( $>16$ ) and ultrashort pulses ( $<0.1$  ps). In practice neither of these limits has been approached. The key reason was believed to be dispersion in the index of refraction in a semiconductor laser. Such dispersion leads to unequal mode separation and ineffective locking.

Prior to the beginning of this program there had been studies of the mode locking behavior of semiconductor lasers to exploit their beneficial properties. The best results achieved had been those reported in [1] with a colliding pulse mode locked (CPM) laser. In these devices, two counter propagating pulses collide in a center saturable absorber to saturate the loss in this device. The presence of the two pulses increases the power available to saturate the absorber on the leading edge of the pulses and thus to effectively shorten the pulses. In this work a pulse width of  $\sim 1$  ps was achieved with approximately 8 locked modes.

The objective of this program was to improve on these results by designing a cavity with minimal round trip dispersion and with minimal dynamic phase dispersion. This was to be accomplished by varying the gain peak and thus the index dispersion on a local basis along the cavity by using a spatially varying energy gap in the active region. It is believed that such a gain region can be grown using selective area epitaxy and that the cavity can be designed to minimize static and dynamic phase dispersion. To accomplish this objective a program in which extensive theoretical modeling was to be undertaken to guide the device design and the experimental research. Furthermore a program of experimental research in which studies of selective epitaxial growth to form the spatially varying active region were undertaken to augment device design, fabrication and evaluation experiments.

## 2.0 Experimental Studies

### 2.1 Laser design

The basic laser design to be used in this study is the colliding pulse mode locked (CPM) laser shown schematically in Figure 1. It consists of a gain region, G, a modulator region, M, and a saturable absorber region, SA. These regions may be sequentially placed along the cavity or positioned symmetrically about the centered SA as shown in the diagram.

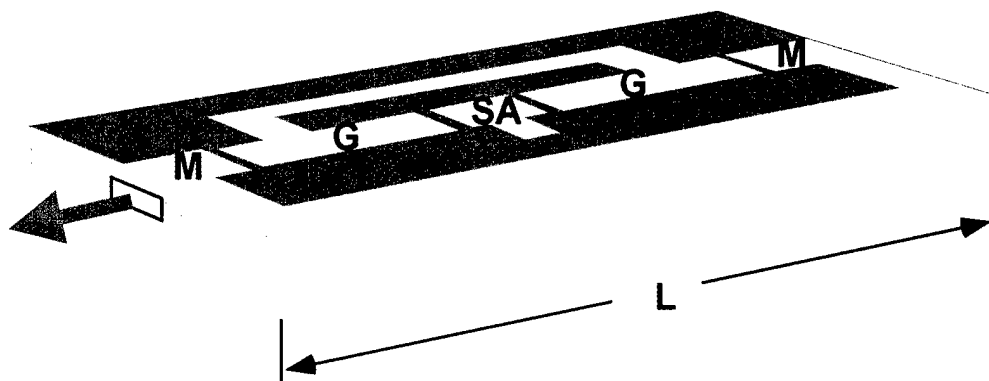


Figure 1 Schematic diagram of CPM laser to studied in this program. G are the gain sections, SA the saturable absorber, and M the modulators.

Symmetric placement is preferred to produce the shortest pulse performance. In this device design the gain regions provide amplification for the optical wave, the modulator sections provide a time dependent loss the frequency of which is matched to the round trip frequency of the light wave,  $c/2nL$ , and the SA region provides an intensity dependent loss mechanism to sharpen the leading edge of a propagating pulse. The waveguide of the device is formed either by forming a buried heterostructure (as schematically illustrated) or through the use of a ridge waveguide. Individual contact is made to each of the regions of the device and the contacts common are interconnected to the same contact pad. The contact pads are isolated from the substrate by an insulating  $\text{SiN}_x$  layer.

The specific lengths of the individual regions was to be determined by experiments and analytical modeling. The total length of the device was chosen to coincide with a round trip frequency of 40 GHz. This resulted in a longitudinal mode separation of 80 GHz since a symmetric CPM device operates with a mode separation twice that is twice the round trip frequency. 40 GHz was also the limit of available RF generators for the modulator drive.

The active region of the device is formed by growth of strained multiple quantum well (QW) layers designed to emit at  $1.55 \mu\text{m}$ . A significant part of the program was designed to exploit selective area growth (SAG) to be able to tailor the active regions to optimize device performance. This will be described in detail in the next section. However, the basic principle involves varying the QW thickness on a spatial scale sufficient to vary the effective energy gap of the device regions to optimize their function in the device operation. This is accomplished by patterning a dielectric layer placed on the wafer prior to growth of the active region. The pattern is chosen to mask the region around the areas in which growth is to occur. Owing to suppression of the growth in the mask regions some of the materials that would have deposited there transport in the vapor and on

the surface to enhance the growth rate in the openings. The growth rate enhancement is determined by the relative dimensions of the open and masked areas and leads to thicker quantum wells with smaller effective energy gaps. By tailoring the pattern, we can then control the effective bandgap in the active region spatially. For example, It may be desirable to increase the energy gap of the saturable absorber to allow it to be operated at higher voltage for rapid sweep out of the carriers. Similar considerations may apply to the modulator. The next section describes the work accomplished in this program to allow us to selectively grow the various regions of the device.

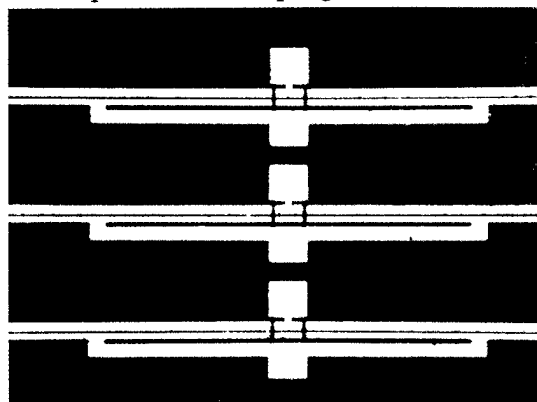


Figure 2 Top view of CPM Modelocked lasers made in this program



Figure 3 View of edge of laser bar showing precision cleave grooves

The fabrication of the device used standard procedures except for controlling the length of the device. Ridge waveguides were fabricated by dry etching a ridge to define the waveguide down to an etch stop layer above the guide layers of the structure. The structure was covered by  $\text{SiN}_x$  and openings for the contacts to the stripes were defined and etched. Ti/Pt?Au ohmic contacts were applied to the surface through a photoresist mask and the residual metal was lifted off to define all of the metal contacts to the various regions simultaneously. Openings to define position of subsequent cleaves were then made in the wafer. These openings were narrow stripes aligned perpendicular to

the cavity at the prescribed separation to yield a 1 mm device. An etchant that defines (111) planes during etching was used to form sharp V-grooves at the position of the openings. These V-grooves act as stress risers during the subsequent cleaving operation and yield devices lithographically controlled lengths. The wafer was then thinned from the back to  $\sim 100$   $\mu\text{m}$  and n-type ohmic contacts were applied to the back of the device. At this time the wafer was cleaved bars by applying bending stress to the wafer. Each bar contains several devices that can be subsequently sawn from the bar or probe-tested.

Figure 2 shows a micrograph of three lasers prior to cleaving.

These lasers are designed to be passively modelocked devices and thus have no modulator sections. The saturable absorber is 40  $\mu\text{m}$  long. Figure 3 shows the end of a bar of devices that have been cleaved using the V-groove location control technique.

## 2.2 MATERIALS GROWTH

### 2.2.1 Calibration of growth with TBAs and TBP

Significant progress towards the required selective area materials technology to fabricate lasers with spatially varying energy gap along the active region was made during the course of this program. Selective area growth involves the patterning of the wafer with an amorphous dielectric to inhibit growth in certain areas. The growth in adjacent areas is then enhanced because they receive a greater supply of reactants. Inhibition of growth in the masked areas cause reactants that would otherwise deposit on the masked areas to diffuse laterally in the gas phase or migrate on the surface to be incorporated in the unmasked areas. This is shown schematically in Fig.4. The mask

dimension,  $w_m$ , relative to the open area,  $w_o$ ,

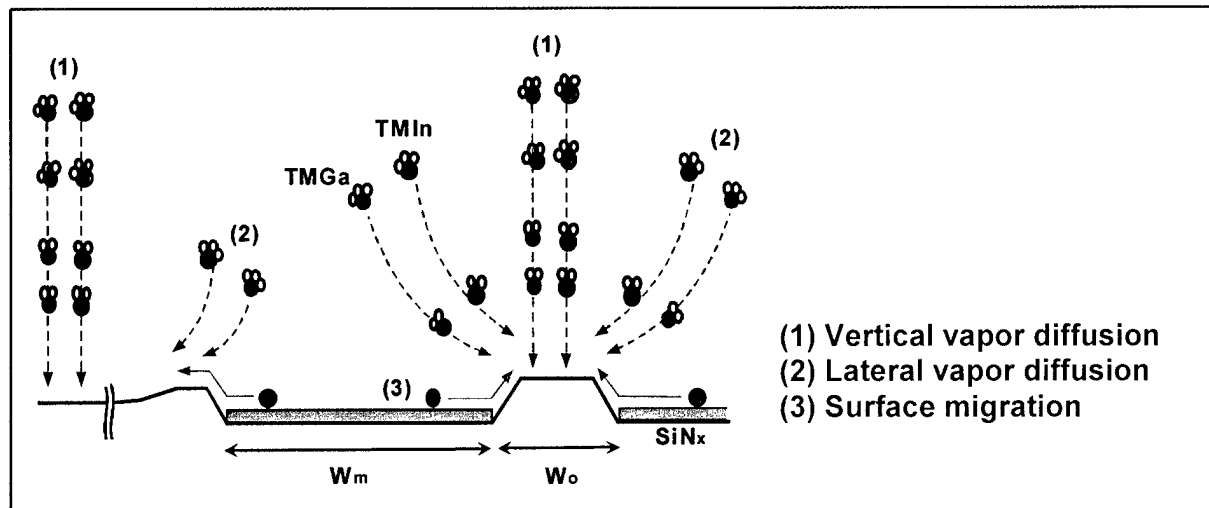


Figure 4 Schematic diagram showing the mechanisms operating in SAG to produce enhanced growth rate on the mask opening.

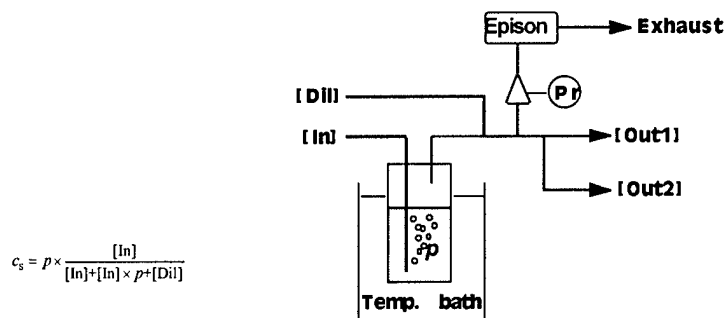


Figure 5 Typical bubbler design for MOCVD sources with multiple outputs.

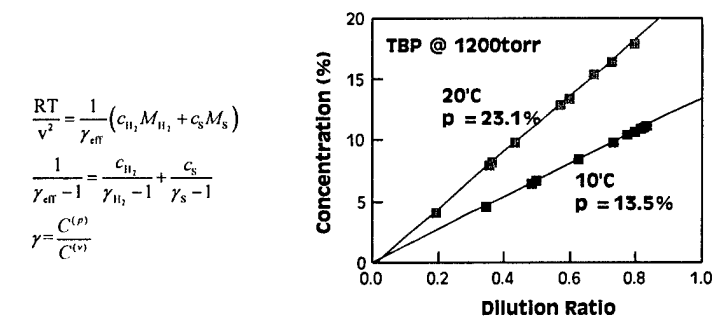


Figure 6 TBP bubbler pickup efficiency vs. flow rates

determines the enhancement of the growth rate in the open area over that which would be observed for an unmasked substrate. Because the various constituents of the lattice diffuse and migrate at different rates, there is also the possibility of a composition change that accompanies this selective growth. To understand the degree to which such effects occur it is important to carefully calibrate the flux of reactants in the system. This is particularly important for our reactor since we are using organometallic reactants for all of the sources, trimethylindium (TMIn), trimethylgallium (TMGa), tertiarybutylarsine (TBAs) and tertiarybutylphosphine (TBP). A careful study of the transport of TBP in arsine was carried out because the growth system involved a dilution system to be able control the TBP flux over a wide range. This portion

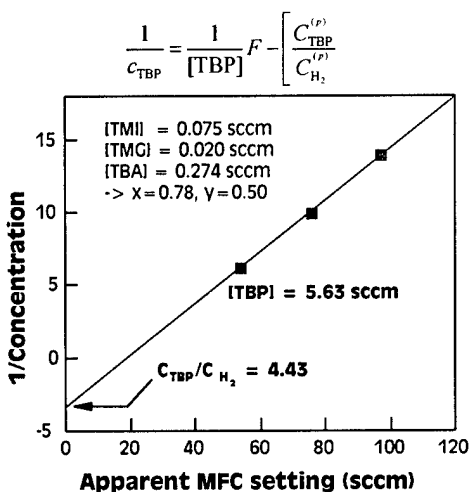


Figure 7 Calibration of TBP bubbler with epison.

series of InGaAsP samples of the same composition under different TBP flow conditions. Since all other variables are fixed, the amount of TBP entering the reactor was known to be the same for all samples. The data and appropriate calibration equations are shown in Fig. 7. This data can only be interpreted if the specific heat of the TBP is 15.3 R. Theoretical calculations also predict the heat capacity to be 15.5R, an excellent agreement. These experiments are crucial to our knowing the

absolute mole fraction input of TBP and TBAs.

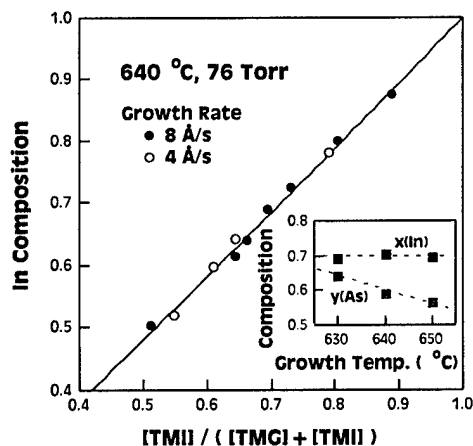


Figure 8 Calibration of the In composition of the Q material vs. gas phase composition.

appropriate structures on planar substrates as well. For example, we expect the column III composition to be linearly dependent on the gas phase reactant ratio. This trend is clearly shown in Figure 8, where the In composition and the As composition of quaternary materials are plotted as a function of the gas

of the system is shown schematically in Fig 5. Passing a carrier gas, [In], through the TBP liquid, the saturated carrier is diluted with another flow of carrier gas, [Dil], to reduce and control the concentration of the TBP in the carrier gas. This diluted gas stream is then sampled by the Epison to measure the concentration of TBP in the gas and the output is split between two out put mass flow controllers , [Out1] and [Out 2]. Since these mass flow controllers were not specifically calibrated for TBP and detailed calibration is necessary to determine the precise flow of TBP that enters the reactor. The pickup from the bubblers was measured by determining the concentration of reactant in the gas flow from the bubbler for flows and temperatures. This data shown in Fig. 6 indicates that pickup of TBP is linear with the dilution flow over the useful range. The output mass flow controllers were calibrated by growing a

The absolute mole fractions of the reactants are very important variables to develop an understanding of the selective area growth enhancement on patterned substrates and to predict the conditions to grow

$$\text{As/P-Efficiency} = \frac{(As/P)_{\text{solid}}}{(As/P)_{\text{vapor}}} = \frac{y}{1-y} \times \frac{[TBP]}{[TBA]}$$

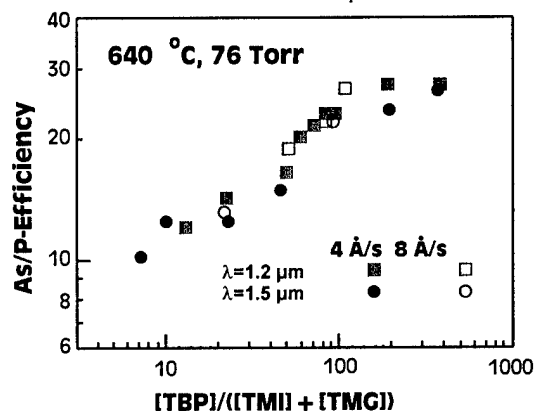


Figure 9 As/P efficiency in the solid vs. V/III ratio.

phase composition and the growth temperature at a fixed gas phase composition, respectively. The close correlation of the data with the expected behavior results because of the accurate calibration we achieved in these studies.

The column V composition, however, is a much more complicated function of the growth parameters. In Figure 9, the V incorporation efficiency is shown as a function of the TBP / III gas phase ratio. The data show that the As incorporates more efficiently at higher TBP mole fractions independent of the growth rate for either 1.2  $\mu\text{m}$  or 1.5  $\mu\text{m}$  materials. This makes control of the composition, and thus strain, a complicated function of the growth parameters.

### 2.2.2 Quantum Well Growth

To achieve reproducible growth of quantum well active regions, we have chosen a design that requires the use of two Q compositions and InP. This design is shown in Figure 10. The quantum wells consist of Q( $\lambda=1.7 \mu\text{m}$ ) wells and Q ( $\lambda = 1.2 \mu\text{m}$ ) barriers. The 1.5  $\mu\text{m}$  emission is achieved by controlling the quantum size effect through the well thickness. The Q ( $\lambda = 1.2 \mu\text{m}$ ) barriers insure that a high confinement potential exists to confine the carriers at room temperature.

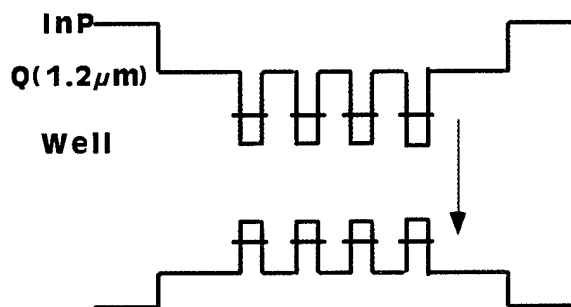


Figure 10 Schematic diagram of MQW structure used in this program.

High quality QW structures have been grown with this design and characterized to calibrate the emission wavelength vs. well thickness. The photoluminescence of three different samples with different well widths are shown in Figure 11. The spectra shown are characteristic of high quality materials. The spectra also show the variation of the emission wavelength as a function of the well width. This is summarized in part b.) of the figure.

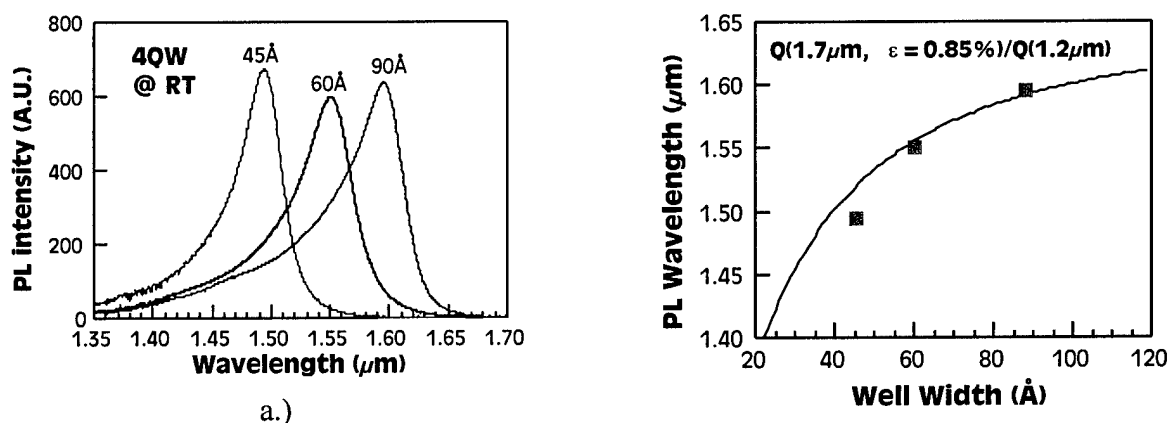


Figure 11 a) PL spectra of QW samples with different well width. B) Plot of emission wavelength vs well width for strained QW layers with 1.2  $\mu\text{m}$  barriers.

The quality of the materials is further verified by the excellent correlation of the X-Ray diffraction spectra measured on these structures as shown in Figure 12. This figure shows the measured and

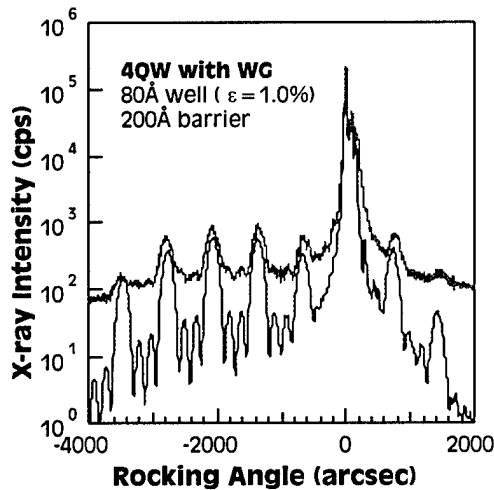


Figure 12 Xray rocking curve of Laser structure.

excellent correlations of peak position and relative intensity attest to the quality of the materials.

Figure 13 shows the PL spectrum of a MQW sample grown with the appropriate structure to emit at 1.55  $\mu\text{m}$ . The sample exhibits a very narrow linewidth indicative of high quality material. Based on these characterizations it was expected that the materials were sufficiently high quality to support the fabrication of high performance devices.

simulated x-ray diffraction spectra from the MQW structures whose PL is shown in Figure 11. The presence of high order diffraction peaks and the

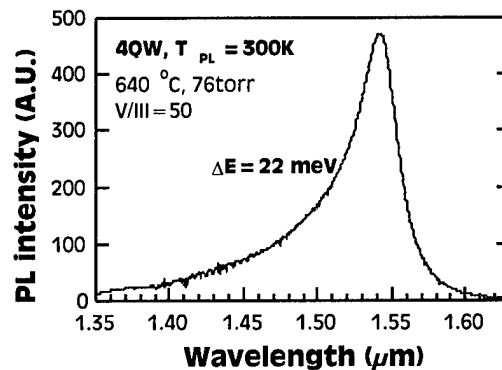


Figure 13 PL spectra of MQW sample showing narrow linewidth

### 2.2.3 Buried Heterostructure Device Fabrication

Since buried heterostructure (BH) lasers are known to exhibit the lowest threshold currents among the many designs available for implementation as a mode locked laser and since the structures are most suitable for implementing single lateral mode designs, effort was devoted to development of these structures for our ML lasers. The key task in fabricating a high quality BH structure is to regrow a current blocking layer over the mesa to be etched in the active region that defines the waveguide. An example of the mesa ridge to be buried is shown in Figure 14. The mesa is deep enough to penetrate the active region of the device and narrow enough to ensure that the resultant mode will be single mode after the mesa is buried in materials with comparable index of refraction. In addition, the burying layers must block current flow so that all of the current flows through the active region. To accomplish this a series of alternately doped

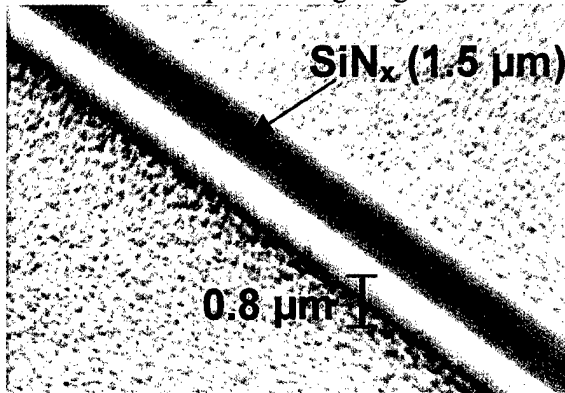


Figure 14 SEM Image of as-etched BH mesa before burying.

layers are grown selectively around the mesa. During the growth of the current blocking layer (CBL), the top of the mesa is covered with  $\text{SiN}_x$  to prevent growth on the top of the mesa. This can result in complicated growth morphology and current leakage paths around the mesa. The desired growth morphology is shown in Figure 15a. Here we illustrate the importance of having the first grown p layer discontinuous with the p layer on the top of the mesa to minimize the possibility of a current leakage path. The two CBL structures shown in the microphotographs of b.) and c.) shown



structures with the N layer of the CBL at  $0.2\ \mu\text{m}$  and  $0.6\ \mu\text{m}$  thickness, respectively. In the latter case note the formation of large growth facets in the n-layer around the mesa. These facets disrupt the subsequent over growth of the top contact layer and apparently create a current path that influences the leakage currents of the device as shown in Figure 16. Here we show the I-V characteristics of these two BH devices. Note the large leakage in the reverse direction and the lower forward turn on voltage of the

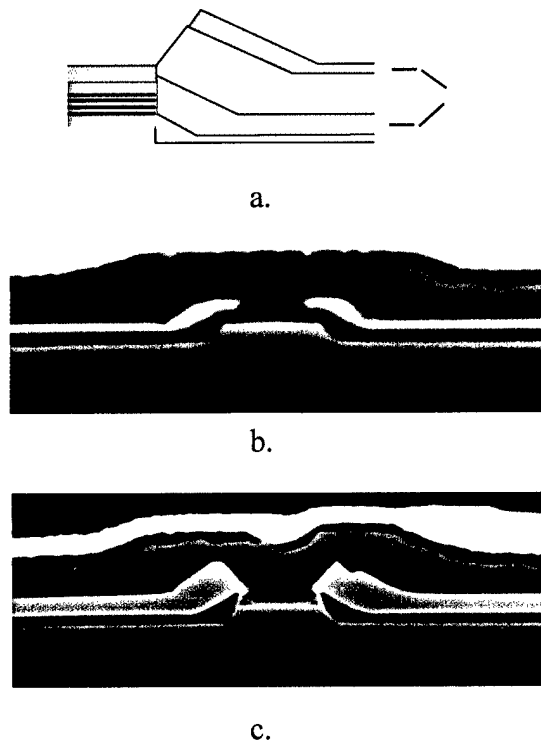


Figure 15 a) Schematic diagram of CBL structure. B) and c) SEM cross sectional images of two BH laser structures

device with the thicker n layer in the CBL. These results suggest the use of thinner n – layers in the CBL.

Optimized CBL layers and device structure as well as the resultant I-V characteristics are shown in

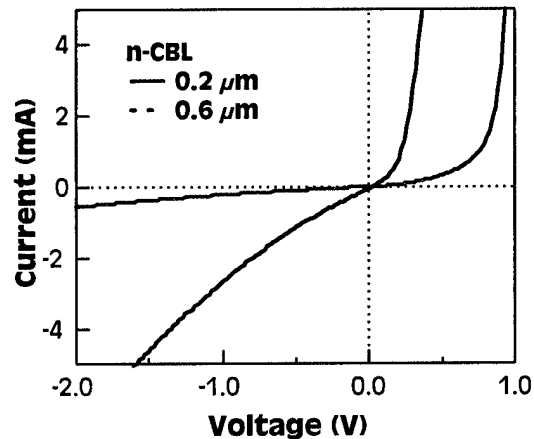
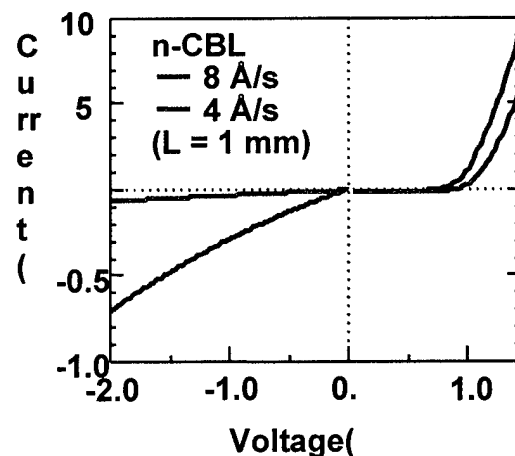


Figure 16 I-V characteristics of BH laser structures showing effect of thick n CBL layer.



a.)



b.)

Figure 17 a) Cross section of BH laser structure. B) I – V characteristics of two devices showing high leakage in device with CBL grown at a high rate.

Figure 17a.) and b.). The data indicate that as long as the n-layer of the CBL is grown at low rates so that its thickness near the edge of the mesa can be controlled, low leakage structures can be grown. These devices result in low threshold room temperature CW operation. The L-I characteristics and spectra of devices operating under CW conditions are shown in Figure 18 a) and b). These devices have 2  $\mu\text{m}$  wide active regions with four QW's. They operated CW with an emission wavelength near 1.55  $\mu\text{m}$ .

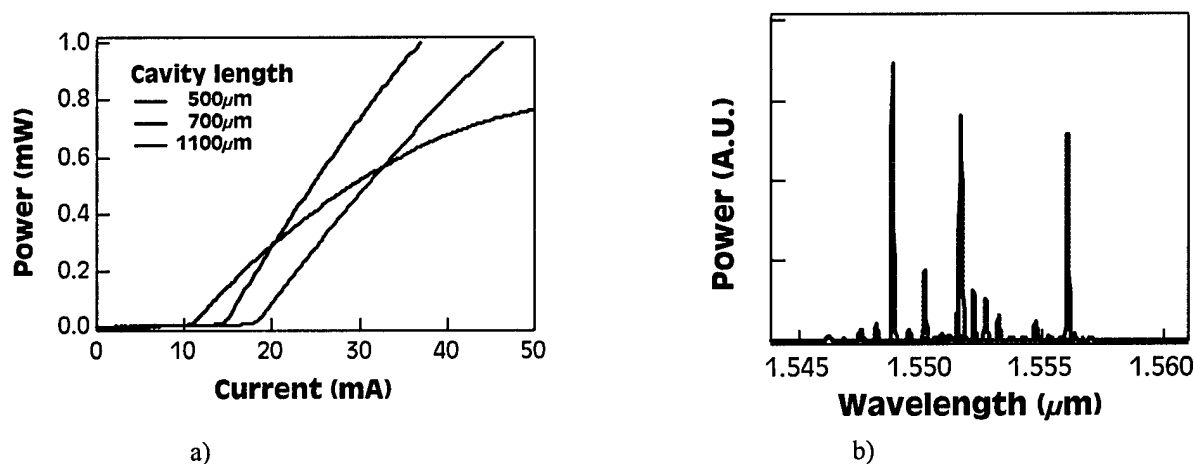


Figure 18 a) Light output versus current for BH lasers of different length. b) Spectra of the same lasers operating under CW conditions.

### 2.2.4 Selective Area Growth

As discussed in the Introduction and in other sections, the program plan called for us to explore the benefits of a spatially varying active region energy gap on the performance of ML lasers. As a result significant experimentation was undertaken in the program to develop techniques for varying the energy gap of the active region along the active stripe use of selective area growth techniques. Although they were not employed in real ML lasers these techniques are central to many integrated device concepts and the results will be applied in many areas.

The basic concept of selected area growth (SAG) is illustrated in Figure 4. A dielectric mask inhibits the deposition of material in certain areas. This increases the growth rate in adjacent areas because the gas phase reactants diffuse to the open areas in the mask driven by a concentration gradient and because reactants that land on the mask migrate over the mask area to the open regions. Gas phase diffusion leads to a more or less uniform increase in the deposition rate over the entire open area, but the surface migration leads to non uniform increases at the margins of the open areas. Owing to surface kinetic phenomena, slow growth planes may be identified in the profile of the deposit in the opening. In Figure 19 we show cross sectional micrographs of an InP deposits on an opening in a mask on an InP substrate. Periodic ultrathin layers of InGaAs are deposited to decorate the growth habit. The two cross sections are markedly different because the opening edges are aligned along different crystalline directions. In 19 a) the stripe openings are aligned along the  $\langle 110 \rangle$  direction. Under these circumstances, slow growth (111A) planes are formed at the edges that define the sidewalls of the mesa. In the orthogonal direction (19 b)), no such plane is present and the crystal grows laterally over the mask.

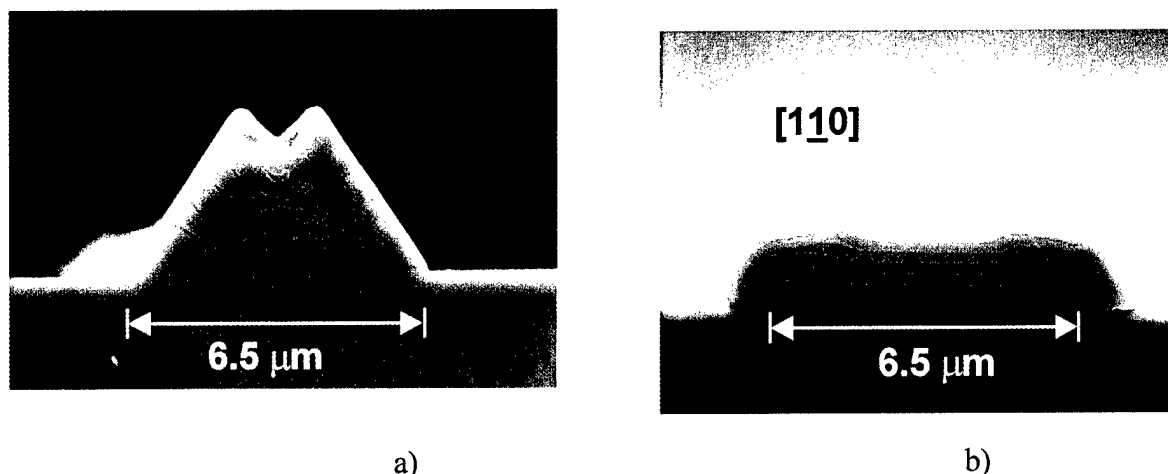


Figure 19. Cross sectional SEM micrographs of selective area growths of InP in stripes oriented along two orthogonal directions in the InP substrate.

In a), the growth habit shows piling up at the edges owing to rapid surface migration and limited (111) plane incorporation. This growth habit leads to self-limited growth and is less useful for device applications than b).

Quaternaries behave differently than InP in selective area growth. There is a stronger tendency for surface migration and the formation of thick “wings” at the edges of the mesa. This is particularly true for the  $\langle 110 \rangle$  oriented stripe. Figure 20 a) and b) shows the growth rate enhancement in the center of a wide stripe for the both  $\langle 110 \rangle$  orientations. The left picture shows the growth rate

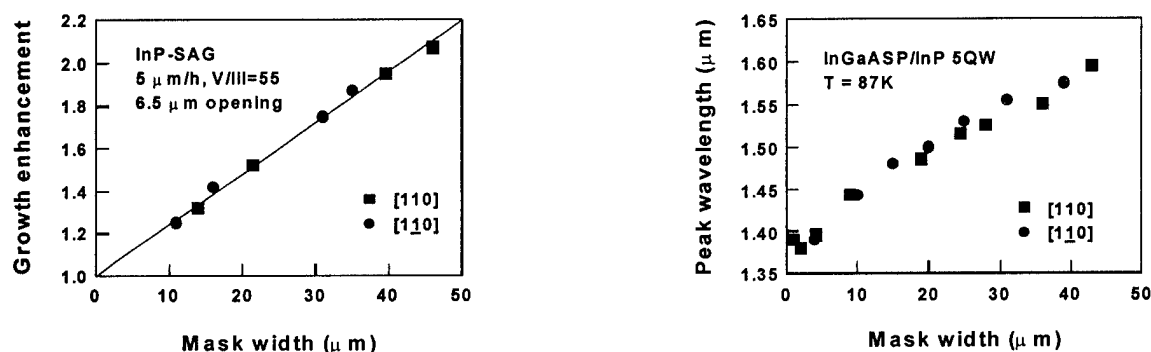


Fig. 20 Growth rate enhancement and QW emission energy for MQW layers grown by SAG on stripes with orthogonal orientations.

enhancement and the right shows the resulting QW emission energy for a QW sample selectively grown in these openings. The independent variable in both cases is the widths of the  $\text{SiN}_x$  mask on either side of the stripe. The wider is the mask, the greater is the growth rate enhancement and the longer is the wavelength of emission. Of course this results from the thicker QW's grown in the stripe opening.

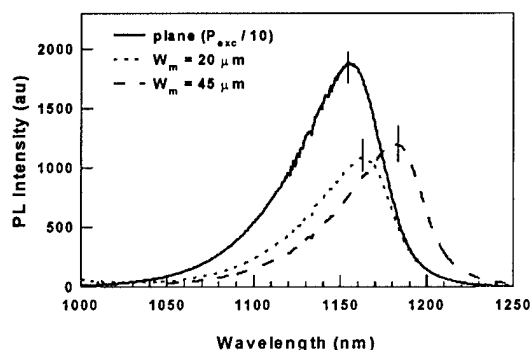


Figure 21 PL of QW samples grown by SAG with two different mask widths showing the shift to longer wavelength with mask width. Note there is little change in the PL intensity in SAG grown materials.

Figure 21 shows the PL spectra of such samples. Note that the linewidths are narrow and PL intensity is high. These data clearly show that variable energy stripes can be formed by varying the width of the mask adjacent to the stripes. Such a capability allows one to design an active stripe with engineered energy gaps in the various regions of the CPM laser.

### 2.3 MODE LOCKED LASER RESULTS

During the course of the program, we were able to demonstrate a state of the art CPM laser using the materials growth technology described above to grow the wafers and by using ridge waveguide designs for the laser. This was chosen to minimize the number of processing steps in the early stages of the device studies while the BH structure was developed. SAG active regions presented an additional processing difficulty that exacerbated our attempts to build BH structure with these active regions. The nonplanarity of the SAG mesa, made it difficult to define  $\sim 1\mu\text{m}$  wide mesas for BH structures on the mesa top. As a result all of the results that are presented in this section were obtained on ridge waveguide structures on planar substrates. In these devices an etch stop layer is included in the structure below the cap layer. A 2-3 micron mesa is defined and etched through the cap and upper confining layer to the etch stop layer which coincides with the waveguide. In addition, small gaps are etched ( $10\mu\text{m}$  long) in the cap layer to provide a measure of isolation between the various segments of the CPM device. All of the devices described in this section were

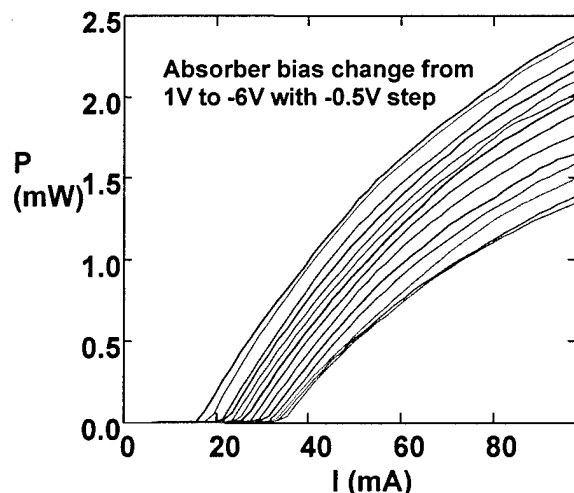


Figure 22 The L-I characteristics of a CPM laser at various absorber biases.

operated as passively mode locked devices as we did not have sufficient RF power in our oscillator to drive the modulator sections and had not yet developed the strip line technology necessary to couple the  $\sim 40\text{ GHz}$  RF into the modulator sections.

Figure 22 shows the L-I characteristics of a passively locked CPM laser for different values of the bias to the absorber. As the bias swings from positive bias to increasingly greater negative values, the threshold of the laser increases. This is to be expected since the absorption at the laser wavelength in reverse biased absorber increases with increasing reverse bias. The threshold current increases

from approximately 16 mA at an absorber bias of 1V to 35 mA at an absorber bias of -6V. The

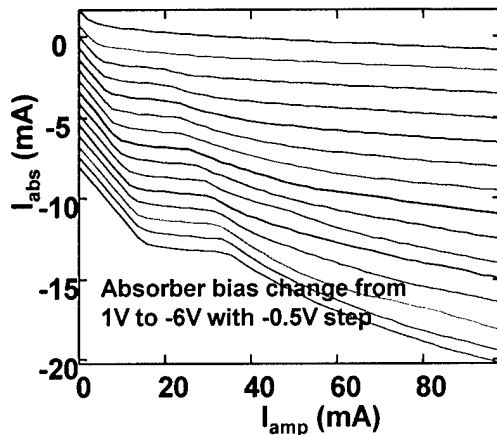


Figure 23 The absorber detected current as a function of the gain section current in a CPM laser.

quantum efficiency of the device also decreases with increasing reverse bias. The increased loss with reverse bias results from the quantum confined Stark effect in the absorber region. The absorption of light in this region results in a current in the absorber contact. This is illustrated in Figure 23, where the absorber current is plotted as a function of the gain section current. The presence of increasing absorber section current with reverse bias at zero gain section current is indicative of leakage between the sections.

Devices like this were tested under a variety of bias conditions. Transient light characteristics were measured using an autocorrelator to measure the pulse width under modelocked conditions. The most reliable measure of CPM was the time averaged spectra. Under modelocked operation, the

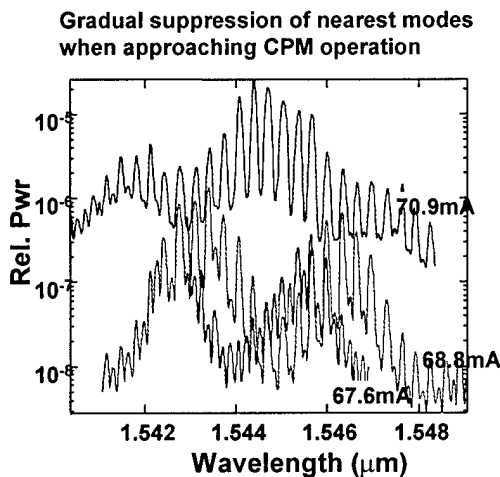


Figure 24 Spectra of modelocked laser under three bias conditions approaching and entering CPM operation.

longitudinal modes lock in phase to produce a repetitive pulsed output in the time domain. Under symmetric CPM operation the degeneracies of the longitudinal modes results in a spectrum with only even modes in the spectrum, i.e. every other mode is missing. A failsafe signature of CPM operation was a spectrum with twice the mode spacing expected for the cavity length. Fig 24 shows the spectra of a CPM laser under different bias conditions. Note that higher forward bias results in the formation of wider mode spacing characteristic of CPM operation. Time domain measurements verified that the device was modelocked under those bias conditions. In general, the range of operating conditions under which CPM operation was observed was narrow for the devices fabricated in this program. The high thresholds observed, the leakage

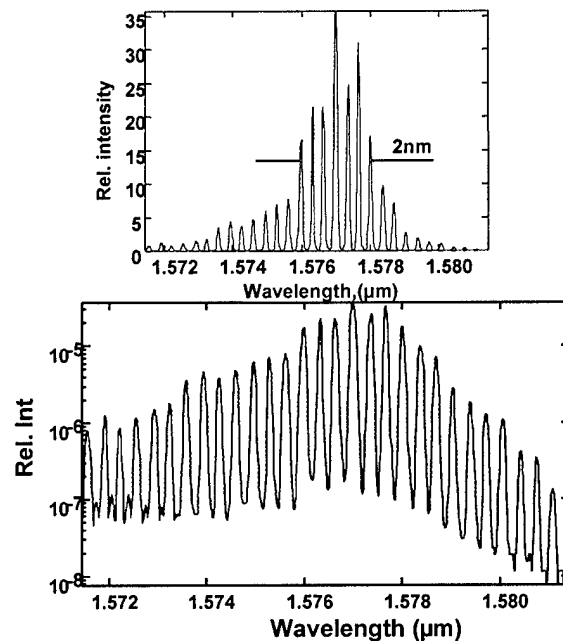


Figure 25 CPM spectra of modelocked laser. The mode spacing is twice the longitudinal spacing expected for the cavity length. This is characteristic of CPM operation.

between segments measured and the use of ridge waveguides led to excessive heat dissipation. In addition, the truncation of the device effort owing to loss of the student involved prevented us from implementing SAG grown active regions to “engineer” the cavity for optimal operation. The analysis of section shows that by balancing the dynamic phase shift in the cavity it is possible to extend the range of passive CPM operation beyond what has been previously achieved. When the bias conditions are optimized, CPM operation over a wide range of wavelengths is observed. Figure 25 a) and b) shows the spectra of the best device we have fabricated operating under the optimal conditions. Double mode spacing is observed over a wide range of wavelengths. These modes are expected to be strongly phase locked and are the wavelength sources that we seek to use in WDM applications. The amplitude of the modes varies strongly with wavelength. Only eight modes have intensities within a factor of two of one another. Nonetheless, these results suggest that with an optimized device the goals of the program can be realized.

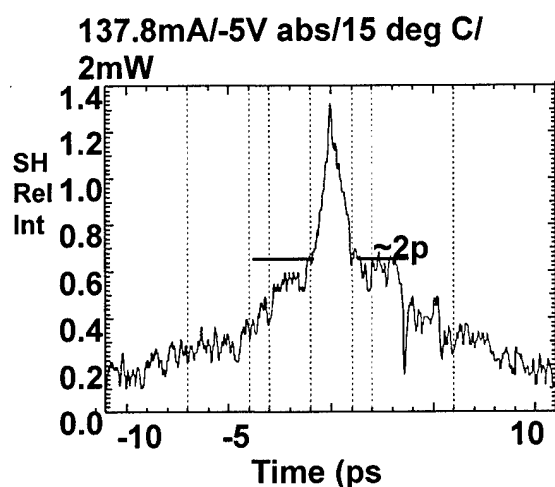


Figure 26 Autocorrelation trace of CPM laser showing a 2 ps FWHM. This corresponds to a 1.2 ps pulse

The time domain characteristics of the output can be measured by using an auto correlation technique. Here the pulse is split and counter propagated through a doubling crystal. The delay between the arrival of the two halves of the pulse is varied to allow them to interact in a region of the crystal under a slit. By varying the delay and measuring the second harmonic radiation through the slit as a function of the delay one can measure the correlation of the pulse with itself. The resultant autocorrelation output shown in Figure 26 shows a pulse width of 2 ps. Deconvolving the pulses from one another, we calculate a pulse width of 1.2 ps. This is equal to the shortest CPM pulse observed in the literature and is consistent with the measure linewidth of the laser mode.

### 3.0 Theory of Passively Mode-Locked Semiconductor Laser under Self Phase Modulation

#### 3.1 Introduction

There has been growing interest in the passive mode locking of monolithic semiconductor lasers to produce higher repetition frequency light sources than allowed by the electrical modulation. High repetition frequencies ranging from hundreds of GHz up to more than THz with sub-picosecond pulses have been demonstrated by shortening the cavity length [1], by employing multiple colliding pulse mode-locking [2], or by employing harmonic mode-locking [3]. Compact in size and self-aligned, the passively mode-locked laser diode operating at 20~100 GHz frequency has potential of the light source without electrical parasitic limitations in the wavelength division multiplexing (WDM) system. Also, the multiple wavelength components in the mode-locked pulse are inherently phase-coherent and equally spaced in the spectrum, which can open a new application in WDM system design [4], [5].

To understand the mode-locking mechanism where the absorption and gain saturation by an optical pulse and their recovery interplay with each other, device simulation is indispensable. In many cases, the electric field propagation through the multi-section cavity is simulated in time domain with the spontaneous emission as a seed, then the steady state after many round trips is investigated [6]-[11]. However, for the monolithic device design with a high repetition frequency ( $>50$  GHz), the mode-locked spectrum contains only several modes separated by more than a few Å's. Also, at high frequency, the complete recovery of the gain or absorption saturation is not allowed, which means that the carrier density modulation is not as deep as the optical modulation. In this case, a frequency domain simulation using the multiple modes as the basis is more attractive than the time domain simulation that can include the spectral dependencies, at best, by gain-spectrum filtering and the group velocity dispersion [7], [9]. The frequency domain method has been used either for qualitative descriptions [2], [12] or in a semi-quantitative way including only the nearest neighbor mode-coupling [13]. In this work, passively mode-locked laser diodes were simulated using the frequency domain method that includes higher order mode coupling than the nearest neighbor coupling and the carrier density dependencies of the gain, carrier recombination rate, and refractive index change. Our recent study [14] showed that the specific carrier density dependencies of the material gain and the carrier recombination rate are the key parameters determining the gain saturation. The line width enhancement factor is also known to be a function of the carrier density and the operation conditions [15]. Therefore, the dependencies of the differential gain, carrier lifetime, and the line width enhancement factor on the amplifier current or absorber reverse bias should be taken into account to predict the device characteristics over a wide operation range. We will show how the inclusion of the self phase modulation (SPM) accompanying the mode coupling reduces the possible operation range of the mode locking and also why the most of the experimental results to date show transform limited pulse width even under SPM. The rate equation for the supermode spectrum is derived in the section 2 with the emphasis on the carrier density dependence of the parameters. The section 3 explains the self-consistency of the solution, numerical procedure for handling the SPM, and the solution stability. The device characteristics simulated under various operation conditions are presented in section 4, which is followed by section 5 for summary.

#### 3.2 Rate equations for a mode-locked laser diode

Schematically shown in Fig. 27 is the model device with a cavity extending over the range  $0 \leq z \leq L$ . The absorber section of length  $h_a L$  is centered at  $(1 + \theta)L/2$ . The rest of the cavity is assumed to be amplifier section. Here, we assume that the total absorption inside the absorber is not high and both facets of the cavity are either as cleaved or high-reflection coated. Under these conditions, the average photon density can

be approximated to be constant over the whole cavity when the intensities of forward and backward propagating waves are summed [16].

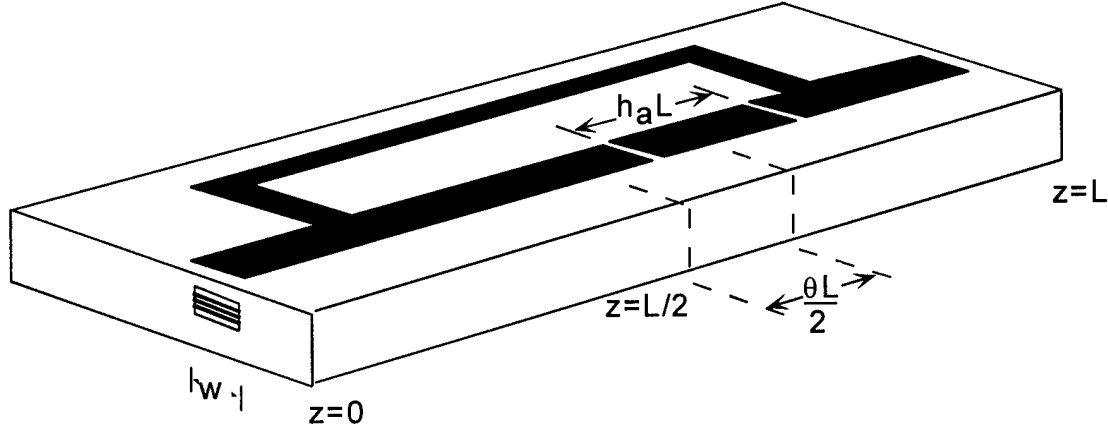


Fig. 27. Schematic figure showing the device dimensions.

The electric field is given by

$$\vec{E}(\vec{r}, t) = \text{Re} \left[ \sum_m E_m(t) e^{i\omega_m t} \vec{a}(x, y) \sqrt{\frac{2}{L}} \cos(\beta_m z) \right], \quad (1)$$

where  $\vec{a}(x, y)$  represents the cross-sectional field distribution and the wave vector  $\beta_m$  satisfies the relation of  $\beta_{m+1} - \beta_m = \pi/L$ . Here, the  $m$ -th mode electric field  $E_m$  is a complex number and slowly varying in time. When the device is uniformly pumped at its threshold, the optical angular frequency is given as  $2\pi\nu_m$ , which is the Fabry-Perot mode of the cavity. When the device is in mode-locked operation, the optical frequencies may be shifted from their original values but they are still expected equally spaced. When  $\delta_0$  is the shift of the central mode ( $m=0$ ) that we arbitrarily assigned at the gain peak, the shift of the other modes can be described by  $\omega_m = 2\pi\nu_m + \delta_0 + m\delta$  so that the repetition frequency  $\Omega$  is given by the relation of

$$\Omega = \omega_{m+1} - \omega_m = 2\pi(\nu_{m+1} - \nu_m) + \delta. \quad (2)$$

The temporal and spatial behavior of the photon density in the active gain or absorber can be obtained by taking the average of  $|\vec{E}(\vec{r}, t)|^2$  spatially over a few wavelengths and temporally over several optical oscillations. This spatial average implies the smearing of the index grating due to carrier diffusion. From (1), the  $z$  and  $t$  dependence of the photon density  $S$  is given by

$$S(z, t) = S_0 \left\{ 1 + \sum_{k>0} 2 \cos\left(\frac{k\pi L}{2}\right) \text{Re} \left[ \tilde{s}^{(k)} e^{i\omega t} \right] \right\}, \quad (3)$$

where

$$\tilde{s}^{(k)} = \frac{\sum_m E_{m+1} E_m^*}{\sum_m E_m E_m^*} \quad (4)$$

represents the depth of the optical field modulation at frequency  $k\Omega$ . To clarify the meaning of  $S_0$ , the average cross-sectional optical power is given as  $E_{ph} \nu_g S_0 (wd)/\Gamma$ , where  $E_{ph}$  is the photon energy,  $\nu_g$  is the group velocity of the light,  $(wd)$  is the cross-sectional area of the active region, and  $\Gamma$  is the optical confinement factor.



The photon density modulation at various frequencies  $k\Omega$  ( $k=1,2,\dots$ ) induces a carrier density modulation at those frequencies described as

$$n = \bar{n} + \sum_{k>0} 2 \cos\left(\frac{k\pi z}{L}\right) \text{Re}\left[\tilde{n}^{(k)} e^{ik\Omega t}\right] \quad (5)$$

Throughout the paper, a quantity with a bar means the average over the time (or DC quantity) and that with a tilde such as  $\tilde{n}^{(k)}$  or  $\tilde{s}^{(k)}$  represents the modulation amplitude at the frequency  $k\Omega$ . It should be noticed that these quantities are different in the absorber and in the amplifier regions.

In the amplifying section under current pumping, the carrier density is related to the photon density through the following rate equation

$$\frac{dn}{dt} = \frac{J_{nom}}{q} - R(n) - v_g S g(n) \quad (6)$$

where  $J_{nom}$  is the volume current density,  $q$  is the electron charge,  $R(n)$  is the carrier recombination rate, and  $g(n)$  is the optical gain. If the carrier modulation terms  $\tilde{n}^{(k)}$  are small enough,  $R(n)$  and  $g(n)$  can be linearly expanded around  $n = \bar{n}$  as in

$$R(n) = R(\bar{n}) + \frac{1}{\tau} \sum_{k>0} 2 \cos\left(\frac{k\pi z}{L}\right) \text{Re}\left[\tilde{n}^{(k)} e^{ik\Omega t}\right] \quad (7)$$

and

$$g(n) = \bar{g} + G \sum_{k>0} 2 \cos\left(\frac{k\pi z}{L}\right) \text{Re}\left[\tilde{n}^{(k)} e^{ik\Omega t}\right], \quad (8)$$

where  $1/\tau = (\partial R / \partial n)|_{\bar{n}}$  and  $G = (\partial g / \partial n)|_{\bar{n}}$ . It should not be overlooked that  $\tau$  and  $G$  strongly depend on  $\bar{n}$  which is also changed by  $S_0$ .

The substitution of (3), (7), and (8) in (6) and reorganizing the terms up to the first order of  $\tilde{n}^{(k)}$  and  $\tilde{s}^{(k)}$  gives the DC operation point determined by

$$\frac{J_{nom}}{q} - R(\bar{n}) - v_g \bar{g} S_0 = 0 \quad (9)$$

and the relationship between the carrier and photon density modulations as

$$\tilde{n}^{(k)} = \frac{-\bar{g} S_0}{(G S_0 + 1/\tau) + ik\Omega} \tilde{s}^{(k)}. \quad (10)$$

For the absorber section, the photo-generated carriers are swept away by the reverse bias, which is better described by the phenomenological time constant,  $\tau_{sw}$ . The introduction of  $\tau_{sw}$  changes (9) to

$$\frac{\bar{n}}{\tau_{sw}} + R(\bar{n}) = v_g (-\bar{g}) S_0 \quad (11)$$

and in (10), the carrier lifetime  $\tau$  in the absorber section should be redefined as

$$\frac{1}{\tau_{(abs)}} = \frac{1}{\tau_{sw}} + \frac{\partial R}{\partial n} \bigg|_{\bar{n}}. \quad (12)$$

These changes make the following derivations applicable to the absorber section as well as the gain section. In the high repetition rate cases that we are mostly interested in,  $\Omega$  is so much larger than  $G S_0$  or  $1/\tau$  that the carrier modulation usually lags the optical modulation by almost  $\pi/2$  and is also small in magnitude, which

validates the linear expansion in (7) and (8). The carrier recovery in the reverse bias in the saturable absorber is described based on the experimental results [17], [18].

The gain and the refractive index modulation due to the carrier density modulation given in (5) is the origin of the mode coupling between the neighborhood modes and the self phase modulation, respectively. The effect of modulating optical gain and the refractive index on a mode can be obtained by the overlap integral of the mode with the polarization [13]. This overlap integral can be separated into the cross-sectional integral and the subsequent longitudinal one along the cavity for heuristic purposes. The cross-sectional overlap integral resulted in

$$\sum_m \left[ \frac{d}{dt} - i(2\pi\nu_m - \omega_m) + \frac{1}{2\tau_{pm}} \right] E_m \cos(\beta_m z) e^{i\omega_m t} = \sum_l \Gamma v_g \left[ \frac{g_l(z, t)}{2} - i \frac{\omega_l}{c} \Delta\mu_l(z, t) \right] E_l \cos(\beta_l z) e^{i\omega_l t}, \quad (13)$$

where  $\tau_{pm}$  is the photon lifetime at  $\omega_m$ , which is determined by the internal loss and the distributed mirror loss, and  $\Delta\mu_l$  represents the refractive index change at  $\omega_l$  from its laser threshold value. Also, the spectral dependence of the gain function is implemented by  $g(n)|_{\omega_l} = g_l(n)$ . The optical confinement factor  $\Gamma$  reflects the fact that the gain and the refractive index change only in the active region of the cross-section. Using the definition of the line width enhancement factor

$$\gamma_l = \frac{(\partial\chi_l' / \partial n)}{(\partial\chi_l'' / \partial n)} \bigg|_{\bar{n}} \quad (14)$$

where  $\chi_l = \chi_l' + i\chi_l''$  is the electric field susceptibility at  $\omega_l$ , the gain and refractive index change for the  $l$ -th mode can be described as

$$\frac{g_l(t)}{2} - i \frac{\omega_l}{c} \Delta\mu_l(t) = \left( \frac{\bar{g}_l}{2} - i\bar{\kappa}_l \right) + i(1 + i\gamma_l) \frac{G_l}{2} [n(t) - \bar{n}], \quad (15)$$

where  $\bar{g}_l = g_l(\bar{n})$  and  $\bar{\kappa}_l = \omega_l \Delta\mu_l(\bar{n}) / c$ . In (15), most of the quantities are position dependent implicitly.

Substituting (5), (10), and (15) in (13) then reorganizing the terms according to their angular frequencies makes it possible to find the rate equation for each mode  $E_m$  which is coupled to the neighboring modes given by

$$\frac{dE_m}{dt} = \left[ -i(\delta_0 + m\delta) - \frac{1}{2\tau_{pm}} + \Gamma v_g \left( \frac{\bar{g}_m}{2} - i\bar{\kappa}_m \right) \right] E_m - \Gamma v_g \frac{\bar{g}}{2} \sum_{k \neq 0} (1 + i\gamma_{m-k}) C_{m-k}^{(k)} \tilde{s}^{(k)} D^{(k)}(z) E_{m-k}, \quad (16)$$

where the mode coupling efficiency  $C_m^{(k)}$  and the modulation field distribution  $D^{(k)}(z)$  defined as

$$C_m^{(k)} = \frac{G_m S_0}{(GS_0 + 1/\tau) + ik\Omega}. \quad (17)$$

and

$$D^{(k)}(z) = \frac{1}{2} + \frac{1}{2} \cos\left(\frac{2k\pi z}{L}\right), \quad (18)$$

respectively. It is noticed that the definitions of  $\tilde{s}^{(k)}$  and  $C_m^{(k)}$  are extended to negative  $k$  indices too by using  $\tilde{s}^{(-k)} = [\tilde{s}^{(k)}]^*$  and  $C_m^{(-k)} = [C_m^{(k)}]^*$ . The spatial average of (16) over the cavity length  $L$  completes the derivation of the rate equation for  $E_m$ 's. When the device cavity is divided into the absorber and amplifier sections whose characteristics are constant in each section, the spatial average can be done very easily by multiplying  $h_a$ , the fraction of the cavity occupied by the absorber, to the absorber parameters and  $(1-h_a)$  to

the amplifier parameters. The explicit position dependence of  $D^{(k)}(z)$  can be reflected by the modification of

$$D_{(abs)}^{(k)} \equiv \int_{abs} D^{(k)}(z)dz = \frac{h_a}{2} \left[ 1 + (-1)^k \frac{\sin(k\pi h_a)}{k\pi h_a} \cos(k\pi\theta) \right] \quad (19)$$

and

$$D_{(amp)}^{(k)} \equiv \int_{amp} D^{(k)}(z)dz = \frac{1}{2} - D_{(abs)}^{(k)} \quad (20)$$

where  $\theta$  is the parameter showing the deviation of the absorber section from the center of the cavity as depicted in Fig. 1. The rate equation for the multimode system can be expressed in the matrix form as

$$\frac{dE_m}{dt} = \sum_l A_{ml} E_l, \quad (21)$$

where  $A_{ml}$  is the corresponding term in (16) after averaging over  $L$ . Simultaneous lasing of many coupled modes can be a steady state solution of system when the matrix  $A$  in the rate equation (21) has the eigenvalue of zero, which is called the supermode. In the simplest case,  $k = \pm 1$  coupling is included, the absorber is located at one end of the cavity by setting  $\theta = 1 - h_a$ , and  $g = G(n - n_0)$  and  $R = n/\tau$  for all carrier density ( $n_0$  is the transparency carrier density), then the steady state of the rate equation (21) can be reduced to the Eq. (33) of Ref. [13].

### 3.3 Simulation procedure

Finding the steady state solution of (21) is restated as an eigenvector problem to find a zero eigenvalue, but solving the problem is much more complicated than it apparently looks. First of all, the set  $\{\tilde{s}^{(k)}\}$  ( $k=1,2,\dots$ ) obtained from the solution  $\{E_m\}$  using (4) should be matched to the corresponding values used in  $A$ . This self-consistency of  $\{\tilde{s}^{(k)}\}$  is the major difference of this problem from the ordinary eigensystems. Among the various eigen-solutions obtained from a given  $A$ , only the one giving self-consistent  $\{\tilde{s}^{(k)}\}$  is meaningful. In numerical pursuit of the solution, we keep following the eigenvector that has the maximum real part of the eigenvalue, and then try to adjust parameters until this eigenvalue becomes zero in both real and imaginary parts. The choice of the maximum real part of the eigenvalue is proposed on the basis that the eigenvalue of  $A$  is interpreted as the change rate of the supermode according to (21), so the supermode with the maximum real part of eigenvalue will dominate finally.

For the self-consistency of  $\{\tilde{s}^{(k)}\}$ , the phase of  $\tilde{s}^{(k)}$  is as important as its magnitude. It seems that the phase of one  $\tilde{s}^{(k)}$  can be arbitrarily changed by the choice of another time reference which changes the relative phase between  $E_m$ 's. However, the use of a different time reference changes the phases of  $\tilde{s}^{(k)}$  in (3), so the solution  $\{E_m\}$  cannot generate the same phase of  $\tilde{s}^{(k)}$  as the input. Therefore, the self-consistency of the  $\tilde{s}^{(k)}$  phase can be achieved only by finding the right solution parameters. Still, to eliminate the ambiguity in choosing the time reference, the phase of one  $\tilde{s}^{(k)}$  is set zero. We usually choose  $k_{ref} = 1$  for this purpose, but the choice of  $k_{ref}$  is not very crucial when several  $k$  numbers are included in the simulation.

In the simulation procedure, the average photon density  $S_0$  is the only independent variable. All the other parameters are interrelated, so they should be solved self-consistently by iteration as well as numerical solution searching procedures. Each iteration step starts with a set of  $E_m$  which is given either by a guess at

first or as the eigenvector solution of  $\mathbf{A}$  from the previous iteration step. The correlation terms  $\{\tilde{s}^{(k)}\}$  for  $\mathbf{A}$  may be preset using this  $\{E_m\}$ . However, at the very beginning of the iteration procedure, the parameters do not generate a self-consistent set of  $\{\tilde{s}^{(k)}\}$  very well. In this case, it is recommended to handle these  $\tilde{s}^{(k)}$ 's as independent parameters instead of as functions of  $E_m$ 's. That is,  $\{\tilde{s}^{(k)}\}$  is arbitrarily adjusted like the other parameters to minimize the difference between the given  $\{\tilde{s}^{(k)}\}$  and the correlation calculated by (4) using the solution eigenvector for  $E_m$  values.

When  $\{E_m\}$  and  $\{\tilde{s}^{(k)}\}$  are given, the average carrier density in the absorber section,  $\bar{n}_{(abs)}$ , is obtained by (11), in which the average absorption  $[-\bar{g}_{(abs)}]$  depends not only on  $\bar{n}_{(abs)}$  but also on  $E_m$  since the average gain  $\bar{g}$  should be defined as

$$\bar{g} = \frac{\sum_m \bar{g}_m |E_m|^2}{\sum_m |E_m|^2} \quad (22)$$

to reflect the spectral dispersion of  $g_m$  in the carrier density rate equation which was oversimplified in (16). The average differential gain  $G$ , which was used in (8), (10), and (17) without clear definition, should be defined in a similar way. Once  $\bar{n}_{(abs)}$  is found for the given  $\{E_m\}$ , all the parameters in the absorber section can be determined from their definitions. The average carrier density in the amplifier section,  $\bar{n}_{(amp)}$ , cannot be directly obtained in the same way as  $\bar{n}_{(abs)}$  since  $J_{nom}$  is unknown yet. Instead,  $\bar{n}_{(amp)}$  should be guessed to set all the gain section parameters, then the  $\delta_0$  and  $\delta$  parameters should be picked up to determine the matrix  $\mathbf{A}$  completely. The eigenvalue with the maximum real part and the corresponding eigenvectors are obtained from  $\mathbf{A}$ , and the resulting  $\{\tilde{s}^{(k)}\}$  is also determined. By iterating  $\bar{n}_{(amp)}$ ,  $\delta_0$ , and  $\delta$  parameters, these three parameters can be best fitted to make both the eigenvalue and the phase of  $\tilde{s}^{(k_{ref})}$  as small as possible. The phase of  $\tilde{s}^{(k_{ref})}$  is mostly affected by the variation of the  $\delta$  parameter, while  $\bar{n}_{(amp)}$  and  $\delta_0$  mostly affect the real and imaginary parts of the eigenvalue, respectively. When these three parameters are best adjusted to minimize the eigenvalue and the phase of the  $\tilde{s}^{(k_{ref})}$ , the new set of  $\{E_m\}$  is obtained from the eigenvector, which completes one iteration step. The iteration process should be repeated until the given  $\{E_m\}$  reproduces itself. When the self-consistent solution is obtained for the given  $S_0$ , the amplifier injection current required to maintain the supermode can be easily calculated from the  $J_{nom}$  in (9). Also the pulse width can be deduced by the Fourier transform of  $\{E_m e^{i(\omega_m - \omega_0)t}\}$  to the time domain. By continuously varying  $S_0$  value then obtaining the solution including  $J_{nom}$ , the device performances can be predicted as functions of the amplifier current.

It should be remembered that there always exists an extra trivial solution that is the single mode lasing whose threshold gain for the amplifier section is the sum of the cavity loss and the absorption in the absorber at the lasing wavelength. When a supermode solution is found with the amplifier carrier density  $\bar{n}_{(amp)}$ , it can be an actual solution only when the gain of any single mode at  $\bar{n}_{(amp)}$  is not higher than its threshold. Therefore, the magnitude of the threshold modal gain reduction with respect to the single mode lasing, which is defined as

$$R_g = \min \left\{ \frac{1}{v_g \tau_{pm}} + [-\Gamma \bar{g}_{m(abs)}] h_a - \Gamma \bar{g}_{m(amp)} (1 - h_a) \right\}, \quad (23)$$

is a good indicator of how much the supermode is more stable than any possible single mode lasing in the system.

In a preliminary study, it was found that a self-consistent solution is very hard to find at some  $S_0$  values when the line width enhancement factor is not negligible. In contrast, the simulation of an imaginary device that does not have any refractive index change shows stable solution over a wide range of  $S_0$  value. The dotted line in Fig. 28 shows one of the typical examples. As the photon density increases, first, the absorption saturation grows to increase the stability of the mode-locked pulse as can be seen in Fig. 2-(a). As the photon density increases further, the increase of the absorber carrier density reduces the differential absorption. As a result, the contribution of the gain saturation starts to compete with that of the absorption saturation, and beyond a certain point, further increase of the photon density starts to decrease the mode-locking stability. Also, because of the time lag between the photon density and the carrier density as is quantitatively described in (10), the absorption and gain saturation introduces phase shift, which can result in the change of the repetition frequency ( $\delta$ ) even without the SPM effect. Of course, in the absence of the SPM, the chirp parameter defined as the second time derivative of the phase of the electric field in time domain is zero. The dotted lines in Fig. 28-(b) and -(c) show these trends. Therefore, the passive mode-locking without the SPM effect is described by the competition between the absorption and the gain saturation, where the carrier density response in phase with the photon density modulation determines the stability of the mode-locking, while the out of phase contribution determines the repetition frequency tuning. Even though not exactly matched, the photon density where the mode-locking stability or  $R_g$  becomes maximum is close to that of zero  $\delta$ , as they are determined by the balance of real and imaginary part, respectively, between the absorber and amplifier contributions.

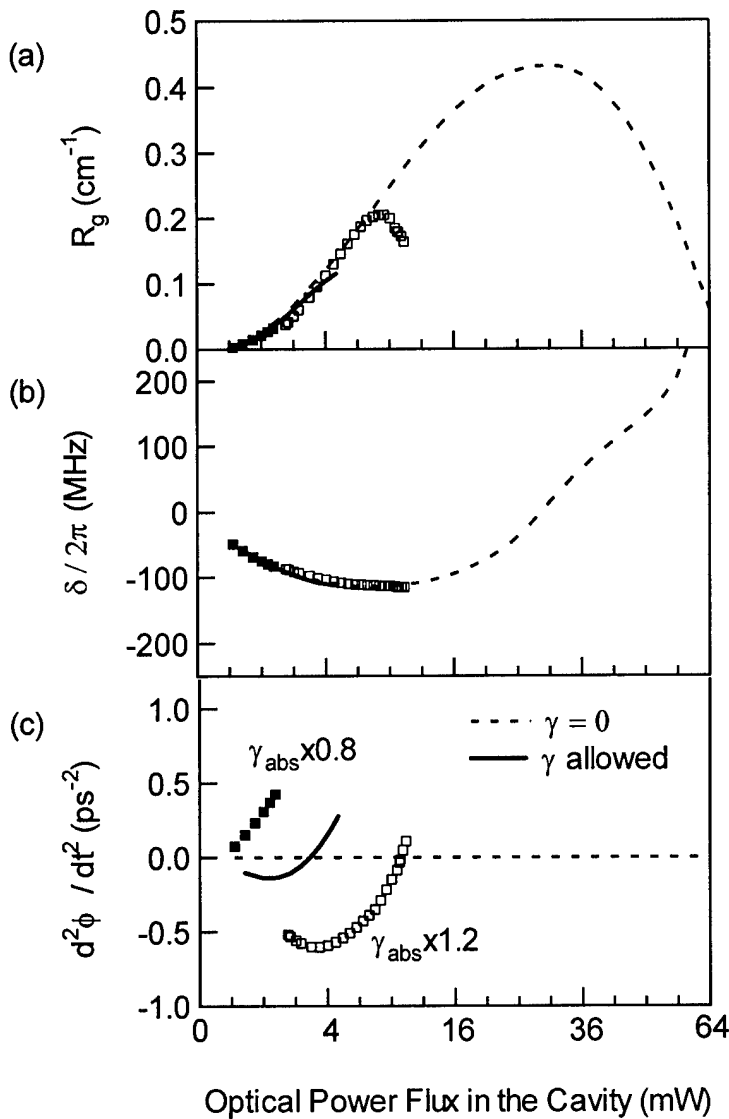


Fig. 28. Effect of the line width enhancement factor on the parameters of (a) mode-locking stability  $R_g$ , (b) repetition frequency shift  $\delta / 2\pi$ , and (c) chirp parameter  $d^2\phi / dt^2$  as functions of the photon density. Dotted and the solid lines are simulated, respectively, in the absence and presence of the line width enhancement factor, while the markers shows the cases where  $\Gamma$  in the absorber section is arbitrarily increased or decreased from the actual value. The optical power is plotted in a square-root scale to clarify the features all over the range. The simulation is performed for a strained 4 quantum-well active region with the parameters of  $L=0.5$  mm ( $\Omega \sim 80$  GHz),  $h_a=0.1$  (located at one end), and  $\tau_{sw}=20$  ps.

The existence of the solution over a wide range of  $S_0$  when the SPM is not allowed can be explained from a mathematical point of view as follows. Keeping in mind that  $G_m$  depends on  $m$  very weakly, the matrix  $A$  is almost Hermitian matrix when  $\kappa_m = 0$  and  $\gamma_m = 0$ . Therefore, the eigenvalues are real and can be sorted according to their magnitude, which makes it unambiguous to pick up the solution. When the SPM is allowed, its contribution can be considered in two ways. When the contribution due to the dynamic modulation of the carrier density is neglected ( $\gamma_m = 0$ ), the inclusion of  $i[h_a\kappa_{m(abs)} + (1-h_a)\kappa_{m(amp)}]$  in the diagonal elements of  $A$  can be just cancelled by a small change of  $\delta_0$  and  $\delta$ , which makes  $A$  Hermitian-like again. This is possible as the refractive index change as a function of the frequency can be approximated as a linear function when the mode-locked spectrum is much narrower than the gain spectrum itself. The small change of  $\delta_0$  and  $\delta$  is the Fabry-Perot mode shift from the uniformly pumped laser as a result of the net index change after a round trip through the amplifier and the absorber sections.

However, when  $\gamma_m$  is allowed, the matrix  $A$  is no longer Hermitian-like and there may exist a couple of eigenvalues whose real parts are close to each other. In this case, because of the supermode competition, a small change in the device parameter can drive the simulation into a completely different result. When the dynamic SPM is allowed through nonzero  $\gamma_m$ , a self-consistent and stable solution can be obtained only when the contribution from the absorber section is partially cancelled by that of the amplifier section. This is possible when the term  $\bar{g}\gamma_m C_m^{(k)} D^{(k)}$  of the absorber and the amplifier sections are almost opposite to each other. In the case of the SPM-free case, the balance between  $\bar{g}C_m^{(k)} D^{(k)}$  terms allowed the maximum  $R_g$  and zero  $\delta$ . As the line width enhancement factor for the absorber is smaller than that of the amplifier because of the difference in the differential absorption and gain, the balance between the dynamic SPM can be achieved at lower power than the maximum  $R_g$  condition of the SPM-free case. When the dynamic SPM is not exactly balanced, the solution stability is at risk and, beyond a certain point, the solution changes discontinuously as the optical power changes continuously, which is the point where the SPM solution (solid lines) is not drawn any further in Fig. 2. In the figure, the  $\kappa_m$  parameters are set arbitrarily zero to facilitate the comparison. Except the chirp characteristics in Fig. 2(c), the  $R_g$  and  $\delta$  parameters are not changed much from the SPM-free solution, because the solution is obtained after the dynamic SPM is balanced between two sections. Also, the chirp characteristics are changed from down-chirp to up-chirp as the optical power increases. When the absorber line width enhancement factor is arbitrarily decreased by 20 %, it is clearly seen that the reducing the dynamic SPM effect of the absorber section shifts the operation range to the lower power side and the pulse becomes more up-chirped. The increase of the absorber dynamic SPM induces the opposite result. The inclusion of the dynamic SPM in the passively mode-locked laser considerably narrows the operating range to the lower power side than the most stabilized, SPM-free case, and the stronger absorber dynamic SPM allows more down-chirp and higher power operation.

In the simulation procedure, the carrier lifetime in the absorber section is mostly determined by  $\tau_{sw}$ , which is not only the strong function of the reverse bias applied on the absorber section but also influenced by the photo-generated carrier screening. Therefore, the simulation over a wide range of optical power with fixed  $\tau_{sw}$  is not completely accurate for the case of a constant absorber reverse-bias. Therefore, the simulation result plotted as a function of the amplifier current with fixed  $\tau_{sw}$  may not represent the device result for a constant absorber bias. However, as the operation range becomes very limited as a result of the dynamic SPM, using a constant  $\tau_{sw}$  for a fixed absorber bias can be justified in the following simulation.

### 3.4 Simulation Result

Using the simulation method described above, we calculated the device characteristics of passively mode-locked lasers of various device structures under various operating conditions. As mentioned in the previous section, there exists a limited operation range in which the simulation gives a stable solution. For example, the absorber recovery time strongly affects the range of the laser current for a stable mode locking. Figure 29 shows the simulation result of the average laser output power as a function of the injection current for a laser with a cavity length of 0.5 mm, where 10% of laser cavity is used for a saturable absorber. By decreasing the sweep time constant or by applying more reverse bias on the absorber section in the real device case, the photo-generated carrier density in the absorber section becomes smaller when a certain amount of light power exists. This means that absorption saturation becomes comparable to the gain saturation at higher optical power than the longer sweep time case. As the stable mode locking is allowed only when the chirp due to absorber section balances that of the gain section, the shorter the sweep time is, the higher is the allowed optical power. Of course, high mode-locked laser power requires high injection current. Therefore, in order to produce a mode-locked pulse power that is high enough for real applications, it is required to apply large reverse bias to accelerate sweeping the photo-generated carriers out of the saturable absorber.

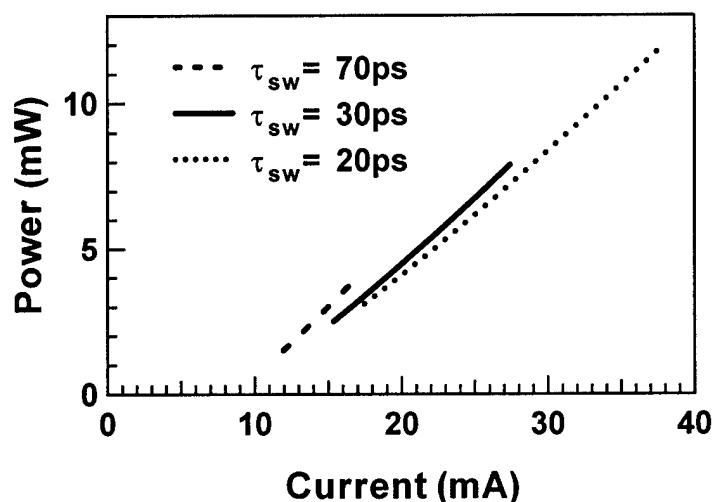


Fig. 29. Simulated mode-locked optical power vs. current relations for different absorber sweep time constant.

The result in Fig. 29 can be rearranged to show the operation current range as a function of inverse sweep time ( $1/\tau_{sw}$ ) that is given in Fig. 30. Here,  $1/\tau_{sw}$  is roughly proportional to reverse bias on the absorber section. This simulation shows almost the same features as the experimental results in Ref. [1]. As can be seen in Fig. 28-(a), the low current side of the stable mode-locking operation current is mostly limited by more stable single mode lasing ( $R_g < 0$ ). Therefore, as the injection current increases, the device operation scheme will change from a single mode lasing to a multi-mode one which is the mode-locked pulse. Meanwhile, the high current side of the mode-locked solution is not limited by the competition with any single mode lasing. In the simulation with SPM for the high optical power, there exist competing multi-mode solutions that are different in amplitude and phase but are very close in threshold gain. Therefore, any small change in the real device operation can shift the operation point from one solution to another. Since all of them are mode-locked pulses, it is expected that pulses will be generated from time to time but without any clear correlation to each other. This is the Q-switched pulse generation. This explanation well matches to the experimental result given in Ref. [1].

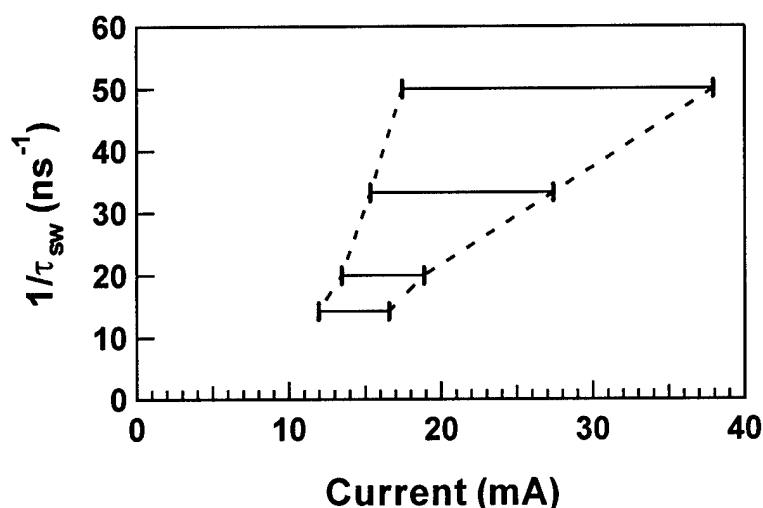


Fig. 30. Simulated device operation conditions giving stable mode-locked pulse.

Because the simulation procedure produces the multi mode spectrum of the mode-locked pulse, the pulse width can be calculated by a simple Fourier transformation of the given spectrum. Figure 31 shows the minimum pulse width that is obtained by adjusting the injection current at each sweep time constant. In the allowed operation range of the injection current for a given sweep time constant, the pulse width depends very weakly on the injection current for most of the cases investigated in this study. This is partly because, within the allowed injection current range, the variation of the absorber carrier density is not large enough to change the relative importance between the absorber and gain sections. However, by decreasing the sweep time constant, the operation optical power increases and the absorber saturation becomes more important in determining the operational balance point. For a given device geometry, narrower pulses can be generated by decreasing the sweep time constant. In a very simplified time-domain explanation of the mode-locked pulse, the role of the saturable absorber is described as absorbing the very beginning part of the pulse and being saturated then letting the rest of the pulse penetrate it after saturation, which cuts off the rising edge of the pulse. In the frequency-domain description, the threshold gain reduction by correlated multi-mode locking is the result of absorption reduction in the saturable absorber. The more number of modes are locked to each other, the narrower becomes the pulse. In order to generate narrower pulse, it is required to drive the device into the condition that allows more absorption saturation. Both descriptions emphasize the role of the strong absorption saturation. Extending this idea further, we compared two device structures with different absorber lengths. In Fig. 31, two mode-locked devices of 0.5 mm cavity length are simulated where the absorber lengths are 5 and 10 % of the cavity length, respectively. It is observed that the device with the longer absorber section generates narrower pulses than the shorter absorber length device does. For an extended cavity mode-locked laser operated at a low repetition frequency, it is believed that the absorber length should be short to generate a narrow pulse. This is based on the postulation that the well-controlled narrow pulse will be spatially confined within the absorber section length. This might be true when tens of picoseconds width pulses are generated from a device with long enough absorber. However, for the passively mode-locked device operated at a very high frequency of ~100 GHz, the pulse period is already comparable to the pulse width so that the realistic pulse is hardly confined inside of the very short absorber. In this case, the minimum pulse width is mostly limited by the amount of attainable absorption saturation, which explains why the longer absorber is more suitable to generate narrow pulses.



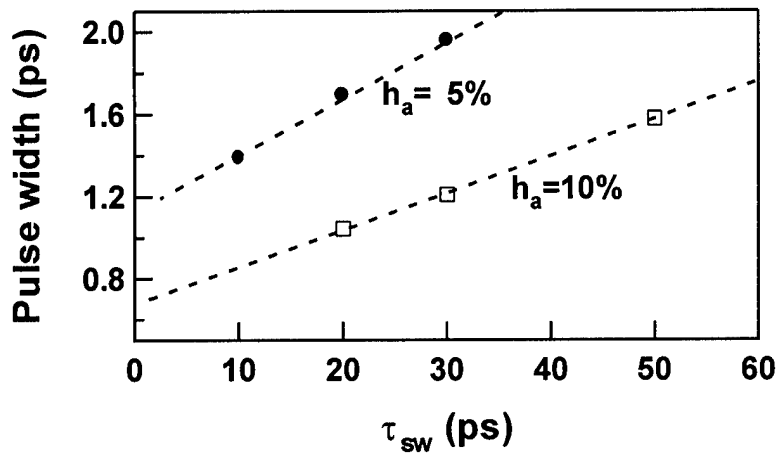


Fig. 31. The minimum pulse width attainable with the given sweep time constant for two different absorber length cases.

### 3.5 Conclusion

We developed a frequency-domain simulation method that is suitable for a high frequency passive mode locking. This method includes the specified carrier density dependencies of the gain and absorption spectra, and also the self phase modulation (SPM) effect due to the refractive index change during the pulse modulation. It is found that the SPM is the major obstacle that limits the high enough power mode-locked pulse output power. Under the effect of SPM, it is shown that the high power operation as well as narrow pulse generation is possible by increasing the absorber saturation effect.

### 3.6 References

- [1] Y.-K. Chen and M. C. Wu, "Monolithic colliding-pulse mode-locked quantum-well lasers," *IEEE J. Quantum Electron.*, vol 28, pp. 2176-2185, 1992.
- [2] J. F. Martins-Filho, E. A. Avrutin, C. N. Ironside, and J. S. Roberts, "Monolithic multimode colliding pulse mode-locked quantum-well lasers: experiment and theory," *IEEE J. Select. Topics Quantum Electron.* vol 1, pp. 539-551, 1995.
- [3] S. Arahira, Y. Matsui, and Y. Ogawa, "Mode-locking at very high repetition rates more than Terahertz in passively mode-locked Distributed-Bragg-reflector laser diodes," *IEEE J. Quantum Electron.*, vol 32, pp. 1211-1224, 1996.
- [4] H. Sanjoh, H. Yasaka, Y. Sakai, K. Sato, H. Ishii, and Y. Yoshikuni, "Multiwavelength light source with precise frequency spacing using a mode-locked semiconductor laser and an arrayed waveguide grating filter," *IEEE Photon. Technol. Lett.*, vol 9, pp. 818-820, 1997.
- [5] H. Shi, G. A. Alphonse, J. C. Connolly, and P. J. Delfyett, "20X5 Gbit/s optical WDM transmitter using single-stripe multiwavelength modelocked semiconductor laser," *Electron. Lett.*, vol 34, pp. 179-181, 1998.
- [6] L. M. Zhang and J. E. Carroll, "Dynamic response of colliding-pulse mode-locked quantum-well lasers," *IEEE J. Quantum Electron.*, vol 31, pp. 240-243, 1995.
- [7] D. J. Jones, L. M. Zhang, J. E. Carroll, and D. D. Marcenac, "Dynamics of monolithic passively mode-locked semiconductor lasers," *IEEE J. Quantum Electron.*, vol 31, pp. 1051-1058, 1995.
- [8] S. Bischoff, M. P. Sørensen, J. Mørk, S. D. Brorson, T. Franck, J. M. Nielson, and A. Møller-Larsen, "Pulse-shaping mechanism in colliding-pulse mode-locked laser diodes," *Appl. Phys. Lett.*, vol 67, pp. 3877-3879, 1995.
- [9] E. A. Avrutin, J. M. Arnold, and J. H. Marsh, "Analysis of dynamics of monolithic passively mode-locked laser diodes under external periodic excitation," *IEE Proc.-Optoelectron.*, vol 143, pp. 81-88, 1996.
- [10] M. Hofmann, S. Bischoff, T. Franck, L. Prip, S. D. Brorson, J. Mørk, and K. Fröjdh, "Chirp of monolithic colliding pulse mode-locked diode lasers," *Appl. Phys. Lett.*, vol 70, pp. 2514-2516, 1997.
- [11] K. Y. Lau, "Narrow-band modulation of semiconductor lasers at millimeter wave frequencies ( $>100$  GHz) by mode locking," *IEEE J. Quantum Electron.*, vol 26, pp. 250-261, 1990.
- [12] O. Solgaard, M.-H. Kiang, and K. Y. Lau, "Pulse buildup in passively mode-locked monolithic quantum-well semiconductor lasers," *Appl. Phys. Lett.*, vol 63, pp. 2021-2023, 1993.
- [13] R. A. Salvatore, S. Sanders, T. Schrans, and A. Yariv, "Supermodes of high-repetition-rate passively mode-locked semiconductor lasers," *IEEE J. Quantum Electron.*, vol 32, pp. 941-952, 1996.
- [14] I. Kim, K. Uppal, and P. D. Dapkus, "Gain saturation in traveling-wave semiconductor optical amplifiers," *IEEE J. Quantum Electron.*, vol 34, pp. 1949-1952, 1998.

- [15] S. H. Cho, C. C. Lu, M. Hovinen, K. Nam, V. Vusirikala, J. H. Song, F. G. Johnson, D. Stone, and M. Dagenais, "Dependence of the line width enhancement factor on the number of compressively strained quantum well in lasers," *IEEE Photon. Technol. Lett.*, vol 9, pp. 1081-1083, 1997.
- [16] M. J. Adams, J. V. Collins, and I. D. Henning, "Analysis of semiconductor laser optical amplifiers," *IEE Proc.*, vol 132, Pt.~J, pp. 58-63, 1985.
- [17] J. R. Karin, R. J. Helkey, D. J. Derickson, R. Nagarajan, D. S. Allin, J. E. Bowers, and R. L. Thornton, "Ultrafast dynamics in field-enhanced saturable absorbers," *Appl. Phys. Lett.*, vol 64, pp. 676-678, 1994.
- [18] M. Hofmann, K. Fröjdh, S. D. Brorson, and Mørk, "Temporal and spectral dynamics in multi-quantum-well semiconductor saturable absorbers," *IEEE Photon. Technol. Lett.*, vol 9, pp. 622-624, 1997.

## 4.0 Program Conclusions and Suggestions For Future Work

The work carried out in this program has demonstrated that it is possible to fabricate ultrashort pulse, wide spectral bandwidth semiconductor modelocked lasers. We also analytically showed that the limiting property of these lasers that prohibits their operation with many ( $> 16$ ) phase locked longitudinal modes is the occurrence of self phase modulation (SPM) in the dynamic operation of the laser. The analysis also shows that for a laser with minimal SPM, i.e.  $\alpha = 0$ , it will be possible to phase lock many more modes and achieve the goal set out in the conception of this program. This zero-SPM condition in principle can be achieved on a round trip basis by careful balancing of the operating points of the various sections of the CPM laser. It is unknown at present whether the zero-SPM condition can be achieved over a broad spectral bandwidth in this way. More extensive modeling will be necessary to determine that bandwidth over which this condition can be achieved.

In this program we have developed the epitaxial tools that will allow us to tailor the energy gap in various segments of the laser to insure that the round trip phase modulation is minimized. We also have shown that high quality devices can be grown using these techniques. What need to be done is to translate accurate models of the device performance to real physical device structures that would allow us to fabricate these devices and test the ideas experimentally. Future programs should undertake this activity.

A second approach that may bear fruit is to design the optical feedback structure of the device so that a part of the SPM is cancelled by a permanent spectral variation in the phase of the reflected wave. This can be accomplished by the use of a grating or photonic crystal mirror in which the reflectance band is positioned so that the high dispersion region compensates the SPM of the device.

Finally, it may be possible to build the device from an active region that is inherently zero SPM. This can be accomplished by the use of an inhomogeneously broadened spectral transition. A quantum dot active region accomplishes this by creating an ensemble of uncoupled spectral delta function emitters. The natural variation of the dot size leads to this spectral dispersion and to the inhomogeneous lineshape. It would be interesting to analyze the consequences of the use of QD active regions in this context and to explore the fabrication of such devices.

## **5.0 Publications and Presentations**

### **5.1 Publications**

In Kim, Dae-Gye Chang, and P. Daniel Dapkus, "Growth of InGaAsP in a stagnation flow vertical reactor using TBP and TBA" J. Crystal Growth vol. 195 (1-4), 138-143 (Dec., 1998).

In Kim, Kushant Uppal, and P. Daniel Dapkus, "Gain Saturation in Traveling-Wave Semiconductor Optical Amplifiers" IEEE J. Quantum Electron. Vol. 34 (10), 1949-1952 (Oct., 1998).

In Kim, Kushant Uppal, Won-Jin Choi, and P. Daniel Dapkus, "Composition control of InGaAsP in metalorganic chemical vapor deposition using tertiarybutylphosphine and tertiarybutylarsine" J. Crystal Growth vol. 193 (3), 293-299 (Oct., 1998).

### **5.2 Presentations at International Conferences**

In Kim, Denis Tishinin, P. Daniel Dapkus, "Control of Selective Area Growth and Regrowth of InP on Mesas by MOCVD Using TBP", The 9th International Conference on Metal Organic Vapor Phase Epitaxy (ICMOVPE IX), La Jolla, CA (31 May-4 June, 1998)

In Kim, Dae-Gye Chang, P. Daniel Dapkus, "Growth of InGaAsP in a Stagnation Flow Vertical Reactor Using TBP and TBA", The 9th International Conference on Metal Organic Vapor Phase Epitaxy (ICMOVPE IX), La Jolla, CA (31 May-4 June, 1998)

In Kim, Won-Jin Choi, and P. Daniel Dapkus, "Stripe Direction Dependence in Selective Area Growth of InGaAsP Using TBP and TBA", Proc. of the 1997 International Conference on Indium Phosphide and Related Materials (IPRM 97), pp 594-597 Hyannis, Cape Cod, MA (11-15 May, 1997) Paper ThB2

In Kim, Kushant Uppal, and P. Daniel Dapkus, "Evaluation of Gain Saturation Behavior in Traveling Wave Semiconductor Amplifiers", Proc. of the 9th IEEE Lasers and Electro-Optics Society Annual Meeting (LEOS 96), vol.2, pp 11-12 Boston, MA (18-21 Nov.,1996) Paper WB3